Supporting Information for:

Chiral Dy(III) single-molecule magnets supported by thiophene-substituted hexaazamacrocycles

Yunquan Wang,[ab] Tingting Wang,[ab] Xiao-Lei Li,[a] Peng Zhang,*[ab] Léo La Droitte,[c] Olivier Cador,[c] Boris Le Guennic,*[c] Zhenhua Zhu*[a] and Jinkui Tang*[ad]

[a] State Key Laboratory of Rare Earth Resource Utilization, Changchun Institute of Applied Chemistry, Chinese Academy of Sciences, Changchun 130022, P. R. China.
[b] School of Applied Chemistry and Engineering, University of Science and Technology of China, Hefei 230026, P. R. China.
[c] Univ Rennes, CNRS, ISCR (Institut des Sciences Chimiques de Rennes)–UMR 6226, F-35000 Rennes, France.
[d] School of Chemistry and Chemical Engineering, Beijing Institute of Technology, Beijing 102488, P. R. China.

Contents

1. Synthesis and characterization.....S2
2. X-ray crystallography data.....S6
3. Magnetic measurements.....S14
4. *Ab initio* calculations.....S28
5. References.....S31

1. Synthesis and characterization

General procedure

Aerobic conditions were applied to all coordination experiments described below. Chiral *ortho*-diamine (1*R*,2*R*)-1,2-di(thiophen-3-yl)ethane-1,2-diamine and (1*S*,2*S*)-1,2-di(thiophen-3-yl)ethane-1,2-diamine were synthesized by enantioselective reductive coupling reaction following a previous work.[1] Other reagents were used as received without any further purification.

Characterization

Elemental analyses (C, H, N, S) were performed by the Perkin-Elmer 2400 analyzer. FT-IR spectra were recorded in the solid state on a Nicolet 6700 Flex FTIR spectrometer equipped with a smart iTR attenuated total reflectance (ATR) sampling accessory in the range from 4000 to 530 cm^{-1}. Powder X-ray diffraction measurements were recorded on Bruker D8 advance X-Ray diffractometer using Cu-Kα radiation. The circular dichroism (CD) spectra in methanol solution were measured on a Jasco J-820 spectropolarimeter at room temperature using quartz optical cells of 10 mm light path length. Thermogravimetric analyses were performed on a Netzsch STA449F3 TG-DSC instrument in the range of 35-800 °C with a heating rate of 10 °C min^{-1} under the N_2 atmosphere.

Synthesis

Synthetic procedure for $[Dy(L^{Thp}{}_{R})(Ph_3SiO)_2][PF_6]$ (**1**)

To a mixture of $DyCl_3{\cdot}6H_2O$ (0.1 mmol, 37 mg) and 2,6-diformylpyridine (0.2 mmol, 27 mg) in methanol (10 mL) was added to (1*R*,2*R*)-1,2-di(thiophen-3-yl)ethane-1,2-diamine (0.2 mmol, 42 mg) dissolved in methanol. The mixture was heated to 70 °C for 5 hours. After the solution was cooled to room temperature, and then the solvent was evaporated under reduced pressure, the brown solid was obtained. The solid was added to the mixture solvents of 15 mL DCM and 15 mL deionized water containing Ph_3SiOH (0.4 mmol, 110 mg), N,N- dimethylethanolamine (0.4 mmol, 40 μL) and $NaPF_6$ (0.1 mmol, 17 mg), and then the mixture was refluxed for 20 min. After being cooled to room temperature, the organic phase was separated and filtered. Pale orange crystals of **1** suitable for single-crystal X-ray measurement were obtained after 2-3 days by layering *n*-pentane on the filtrate at room temperature. Yield: 34 mg, 21% (based on Dy). Elemental analysis (%) calcd for $C_{70}H_{56}DyF_6N_6O_2PS_4Si_2$ (M_w = 1505.13): C, 55.86; H, 3.75; N, 5.58; S, 8.52. Found: C, 55.51; H, 3.68; N, 5.77; S, 8.49. FTIR ν/cm^{-1} (ATR): 3064 (vw), 1652 (w), 1592 (m), 1481 (vw), 1463 (w), 1427 (m), 1270 (w), 1233 (vw), 1168 (w), 1104 (m), 1046 (w), 1030 (w), 1007 (w), 957 (s), 833 (vs), 784 (s), 730 (m), 699 (vs), 652 (m), 637 (s), 555 (s), 536 (w).

Synthetic procedure for $[Dy(L^{Thp}{}_S)(Ph_3SiO)_2][PF_6]$ (**2**)

The same synthetic protocol was used as that of **1** through the replacement of (1*R*,2*R*)-1,2-di(thiophen-3-yl)ethane-1,2-diamine with (1*S*,2*S*)-1,2-di(thiophen-3-yl)ethane-1,2-diamine. Yield: 43 mg, 25% (based on Dy). Elemental analysis (%) calcd for $C_{70}H_{56}DyF_6N_6O_2PS_4Si_2$ (M_w = 1505.13): C, 55.86; H, 3.75; N, 5.58; S, 8.52. Found: C, 55.31; H, 3.68; N, 5.89; S, 8.47. FTIR ν/cm^{-1} (ATR): 3064 (vw), 1653 (w), 1592 (m), 1481 (vw), 1463 (w), 1427 (m), 1270 (w), 1232 (vw), 1168 (w), 1107 (m), 1048 (w), 1030 (w), 1007 (w), 959 (s), 833 (vs), 784 (s), 730 (m), 699 (vs), 652 (m), 637 (s), 555 (s), 536 (w).

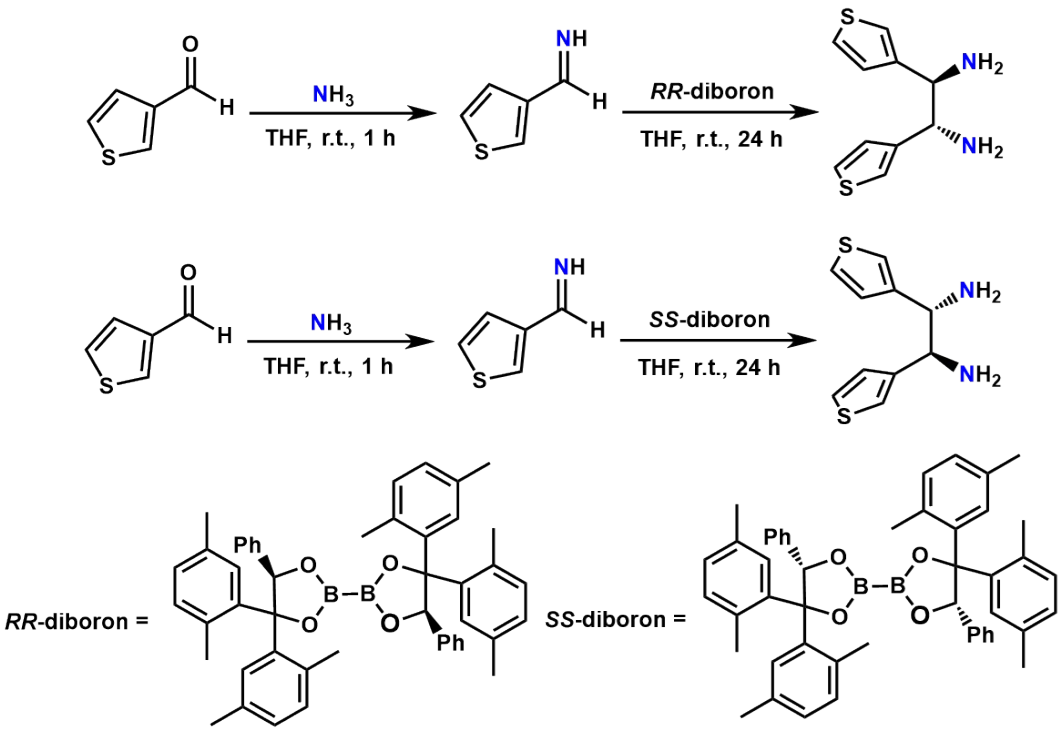

Scheme S1 Synthetic routes for (1*R*,2*R*)-1,2-di(thiophen-3-yl)ethane-1,2-diamine and (1*S*,2*S*)-1,2-di(thiophen-3-yl)ethane-1,2-diamine.

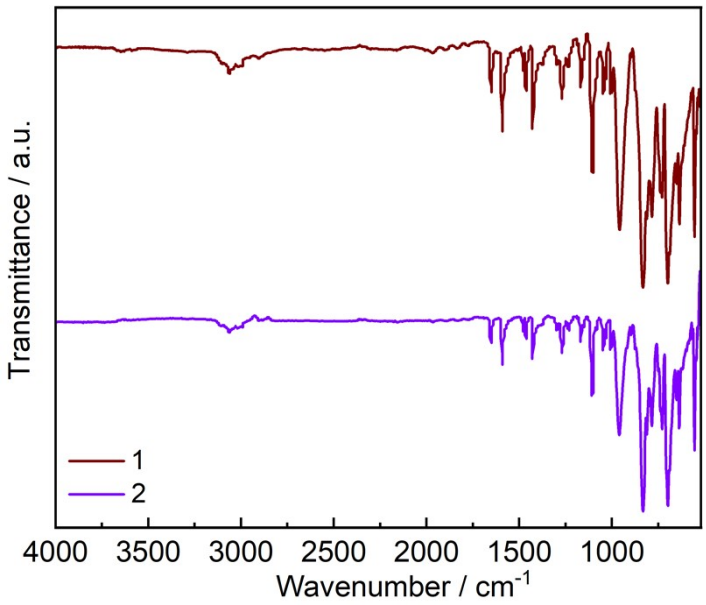

Fig. S1 IR spectra of **1** and **2**.

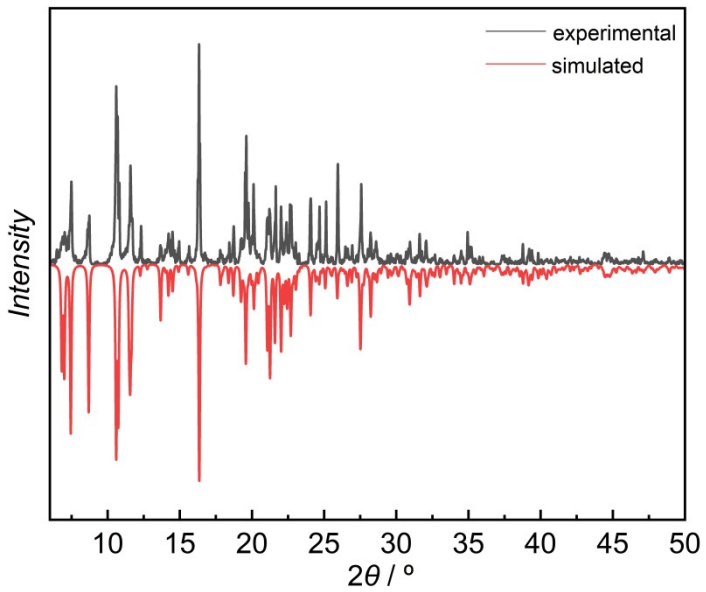

Fig. S2 Powder XRD patterns of **1**: experimental (black) and simulated (red).

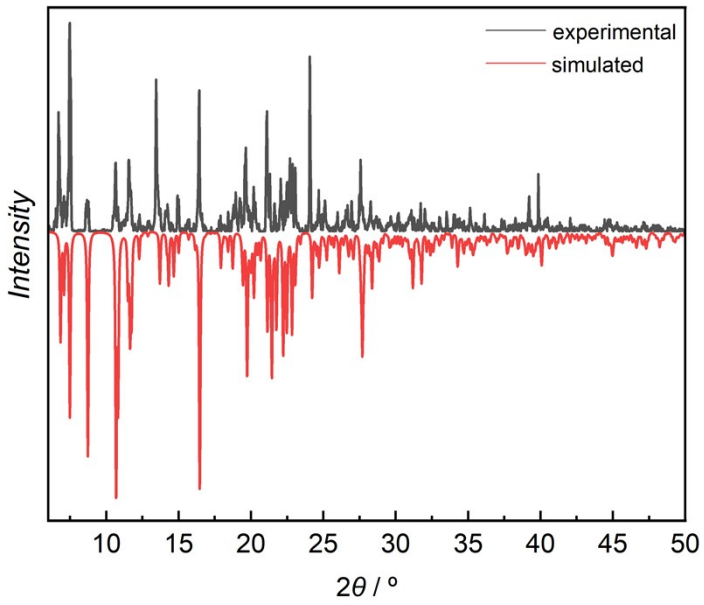

Fig. S3 Powder XRD patterns of **2**: experimental (black) and simulated (red).

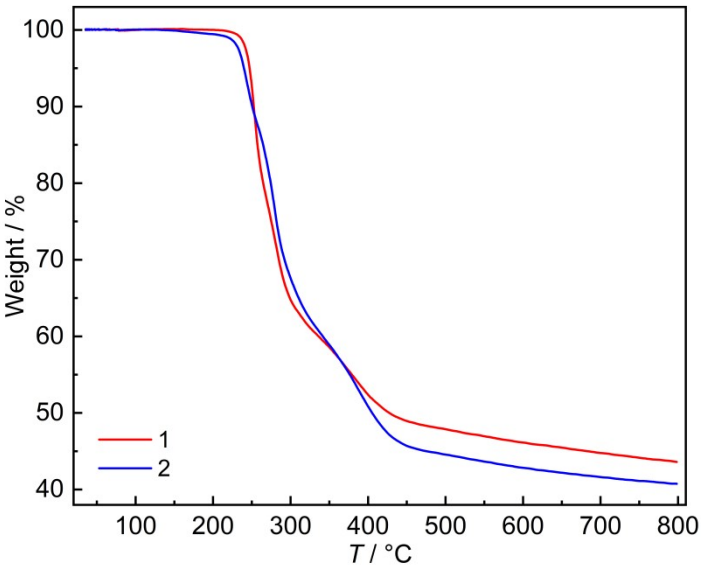

Fig. S4 Thermogravimetric analysis for **1** (red) and **2** (blue).

2. X-ray crystallography data

Single-crystal X-ray data for **1** and **2** were collected using a Bruker D8 Venture CCD diffractometer with graphite-monochromatized Mo Kα radiation (λ = 0.71073 Å) at 302 K and 180 K, respectively. The structures were solved in Olex2 program with SHELXT using intrinsic phasing and were refined with SHELXL using least squares minimization.[2-4] All non-hydrogen atoms were refined anisotropically. All hydrogen atom positions were calculated geometrically and refined using the riding model. Crystallographic data and refinement details are given in Table S1.

Table S1 Crystal data and structure refinements for **1** and **2**.

Identification code	**1**	**2**
Chemical formula	$C_{71}H_{62}Cl_2DyF_6N_6O_4PS_4Si_2$	$C_{72}H_{60}Cl_4DyF_6N_6O_2PS_4Si_2$
Formula Mass	1626.05	1674.95
Crystal system	triclinic	triclinic
a (Å)	10.2790(13)	10.2306(5)
b (Å)	14.016(2)	13.8626(7)
c (Å)	14.385(2)	14.3526(7)
α (°)	64.584(5)	64.489(2)
β (°)	82.661(5)	83.113(2)
γ (°)	83.002(5)	83.204(2)
Unit cell volume (Å^3)	1851.4(5)	1818.75(16)
Temperature (K)	302.0	180.0
Space group	*P*1	*P*1
Z	1	1
ρ_{calc} (g/cm^3)	1.458	1.529
F (000)	823.0	845.0
Radiation	Mo Kα (λ = 0.71073)	Mo Kα (λ = 0.71073)
Reflections collected	26755	33265
Independent reflections	12377	12691
R_{int}	0.0240	0.0508
GOF on F^2	1.096	1.048
R_1 (I ≥2 σ (*I*))	0.0353	0.0422
wR_2 (all data)	0.0999	0.1049
Flack parameter	0.052(4)	0.038(6)
CCDC number	2515622	2515623

Table S2 Selected bond distances (Å) for **1** and **2**.

1		**2**	
Dy1-O1	2.091(8)	Dy1-O1	2.086(9)
Dy1-O2	2.145(7)	Dy1-O2	2.157(7)
Dy1-N1	2.672(8)	Dy1-N1	2.714(10)
Dy1-N2	2.651(9)	Dy1-N2	2.658(12)
Dy1-N3	2.687(7)	Dy1-N3	2.698(9)
Dy1-N4	2.732(7)	Dy1-N4	2.683(10)
Dy1-N5	2.670(10)	Dy1-N5	2.657(12)
Dy1-N6	2.692(7)	Dy1-N6	2.685(9)

Table S3 Selected bond angles (°) for **1** and **2**.

1		**2**	
O1-Dy1-O2	179.4(4)	O1-Dy1-O2	179.3(5)
O1-Dy1-N1	82.4(3)	O1-Dy1-N1	87.2(3)
O1-Dy1-N2	88.5(3)	O1-Dy1-N2	92.2(4)
O1-Dy1-N3	98.6(3)	O1-Dy1-N3	91.6(3)
O1-Dy1-N4	87.5(3)	O1-Dy1-N4	83.0(3)
O1-Dy1-N5	91.9(3)	O1-Dy1-N5	88.2(4)
O1-Dy1-N6	91.9(3)	O1-Dy1-N6	98.3(3)
O2-Dy1-N1	97.9(3)	O2-Dy1-N1	92.3(3)
O2-Dy1-N2	91.5(3)	O2-Dy1-N2	88.0(3)
O2-Dy1-N3	81.2(3)	O2-Dy1-N3	89.1(3)
O2-Dy1-N4	92.2(3)	O2-Dy1-N4	97.4(3)
O2-Dy1-N5	88.1(3)	O2-Dy1-N5	91.6(3)
O2-Dy1-N6	88.3(3)	O2-Dy1-N6	81.0(3)
N1-Dy1-N3	121.1(2)	N1-Dy1-N3	120.7(3)
N1-Dy1-N4	169.9(2)	N1-Dy1-N4	170.2(3)
N1-Dy1-N6	60.6(2)	N1-Dy1-N6	59.7(3)
N2-Dy1-N1	60.4(2)	N2-Dy1-N1	60.4(3)
N2-Dy1-N3	60.8(2)	N2-Dy1-N3	60.4(3)
N2-Dy1-N4	119.1(2)	N2-Dy1-N4	120.8(3)
N2-Dy1-N5	179.4(4)	N2-Dy1-N5	179.0(4)
N2-Dy1-N6	120.4(2)	N2-Dy1-N6	118.4(3)
N3-Dy1-N4	59.8(2)	N3-Dy1-N4	60.7(3)
N3-Dy1-N6	169.4(2)	N3-Dy1-N6	170.1(3)
N5-Dy1-N1	120.1(3)	N5-Dy1-N1	118.7(3)
N5-Dy1-N3	118.7(2)	N5-Dy1-N3	120.5(3)
N5-Dy1-N4	60.5(2)	N5-Dy1-N4	60.2(3)
N5-Dy1-N6	60.0(2)	N5-Dy1-N6	60.6(3)
N6-Dy1-N4	120.5(2)	N6-Dy1-N4	120.7(3)

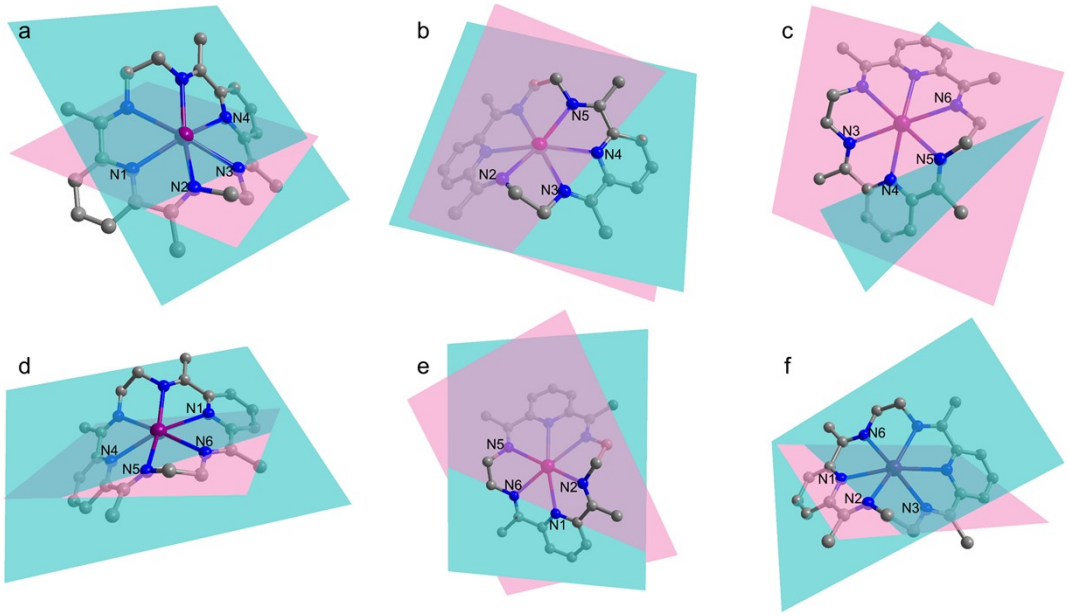

Fig. S5 Dihedral angles (°) in equatorial hexaazamacrocycle for $[Dy(L^{N6})(Ph_3SiO)_2][PF_6]$[5]: (a) N1-N2-N3-N4: 32.64, (b) N2-N3-N4-N5: 11.55, (c) N3-N4-N5-N6: 39.59, (d) N4-N5-N6-N1: 24.16, (e) N5-N6-N1-N2: 18.91, (f) N6-N1-N2-N3: 47.53. Note for example that the dihedral angle N1-N2-N3-N4 is the angle between the N1N2N3 plane and the N2N3N4 plane. Dy, violet; C, grey; N, blue.

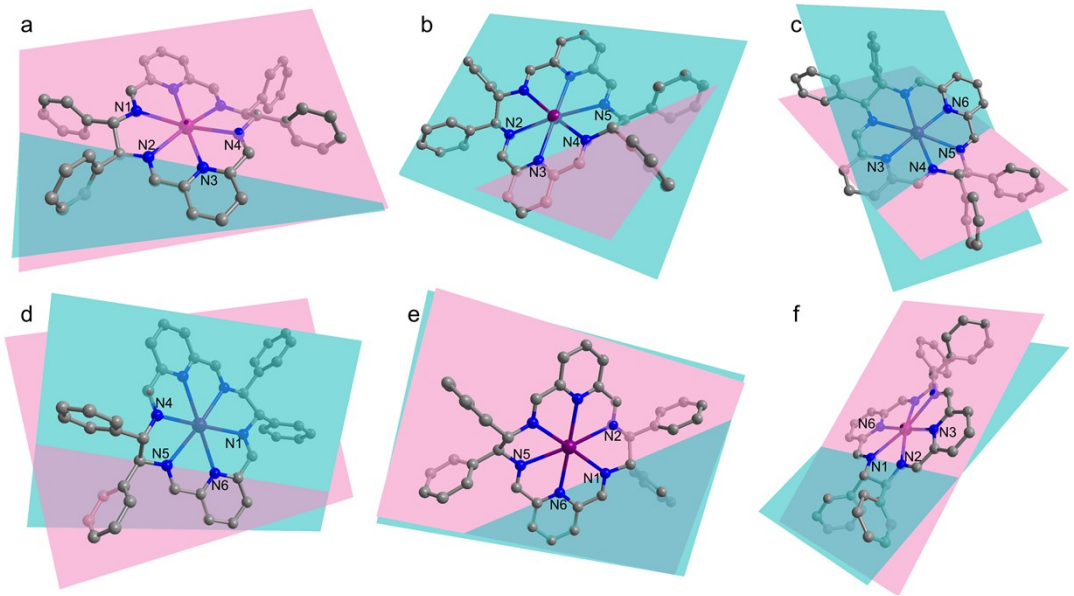

Fig. S6 Dihedral angles (°) in equatorial hexaazamacrocycle for $[Dy(L^{N6}{}_R)(Ph_3SiO)_2][PF_6]$[6]: (a) N1-N2-N3-N4: 5.24, (b) N2-N3-N4-N5: 20.33, (c) N3-N4-N5-N6: 32.84, (d) N4-N5-N6-N1: 21.45, (e) N5-N6-N1-N2: 3.55, (f) N6-N1-N2-N3: 16.87. Note for example that the dihedral angle N1-N2-N3-N4 is the angle between the N1N2N3 plane and the N2N3N4 plane. Dy, violet; C, grey; N, blue.

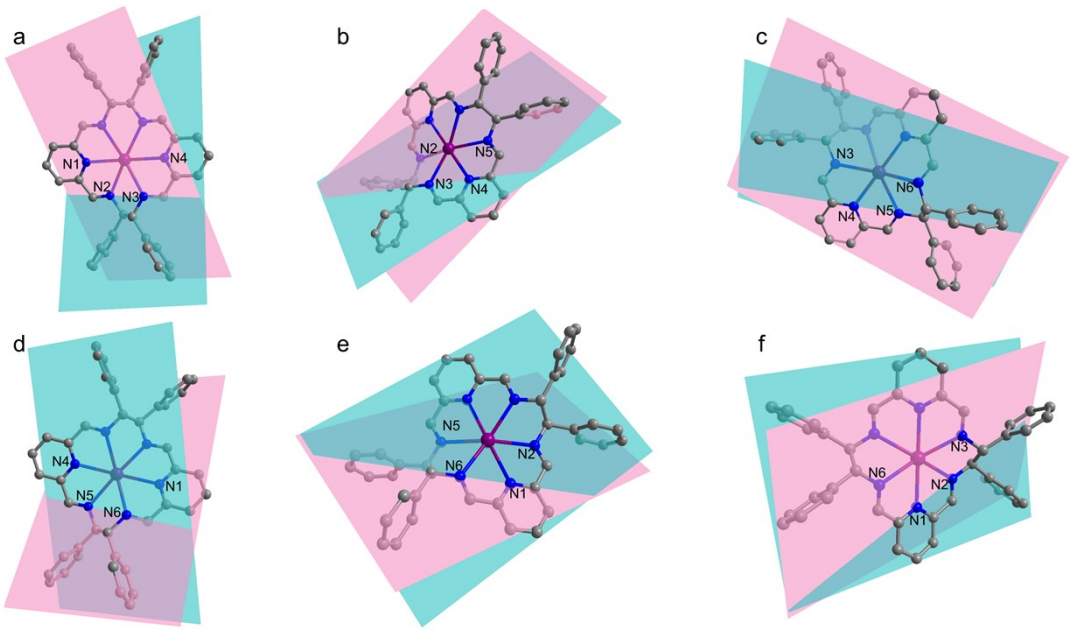

Fig. S7 Dihedral angles (°) in equatorial hexaazamacrocycle for $[Dy(L^{N6}{}_{R})(3ThCOO)_2][BPh_4]$[7]: (a) N1-N2-N3-N4: 45.12, (b) N2-N3-N4-N5: 23.62, (c) N3-N4-N5-N6: 21.06, (d) N4-N5-N6-N1: 44.57, (e) N5-N6-N1-N2: 23.70, (f) N6-N1-N2-N3: 21.63. Note for example that the dihedral angle N1-N2-N3-N4 is the angle between the N1N2N3 plane and the N2N3N4 plane. Dy, violet; C, grey; N, blue.

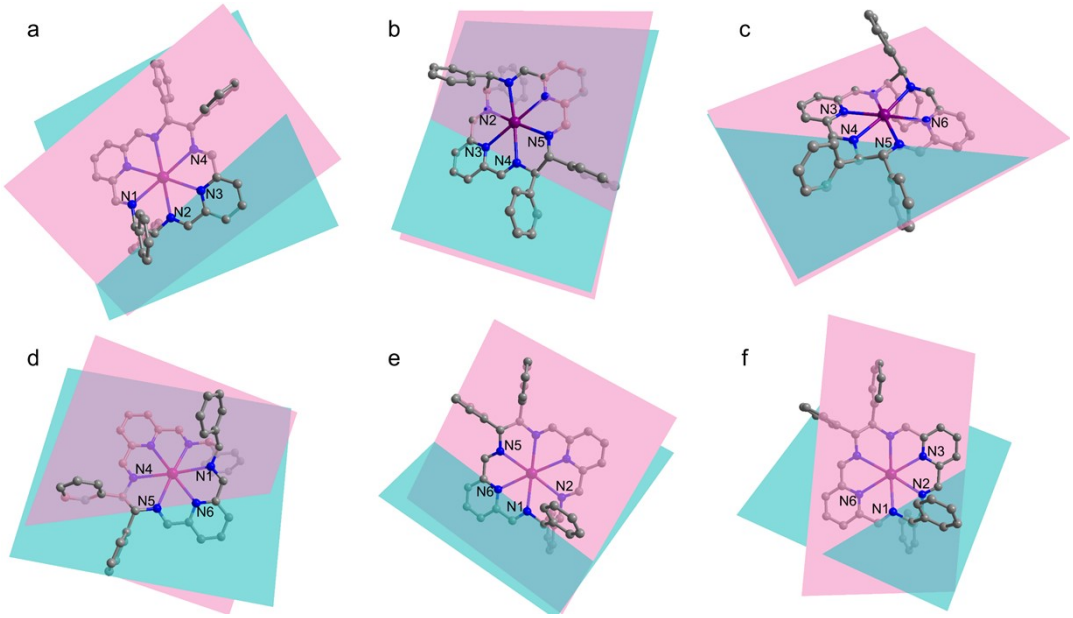

Fig. S8 Dihedral angles (°) in equatorial hexaazamacrocycle for $[Dy(L^{N6}{}_{R})([7]helicene)_2][BPh_4]$[8]: (a) N1-N2-N3-N4: 27.84, (b) N2-N3-N4-N5: 6.86, (c) N3-N4-N5-N6: 3.36, (d) N4-N5-N6-N1: 21.65, (e) N5-N6-N1-N2: 42.40, (f) N6-N1-N2-N3: 44.25. Note for example that the dihedral angle N1-N2-N3-N4 is the angle between the N1N2N3 plane and the N2N3N4 plane. Dy, violet; C, grey; N, blue.

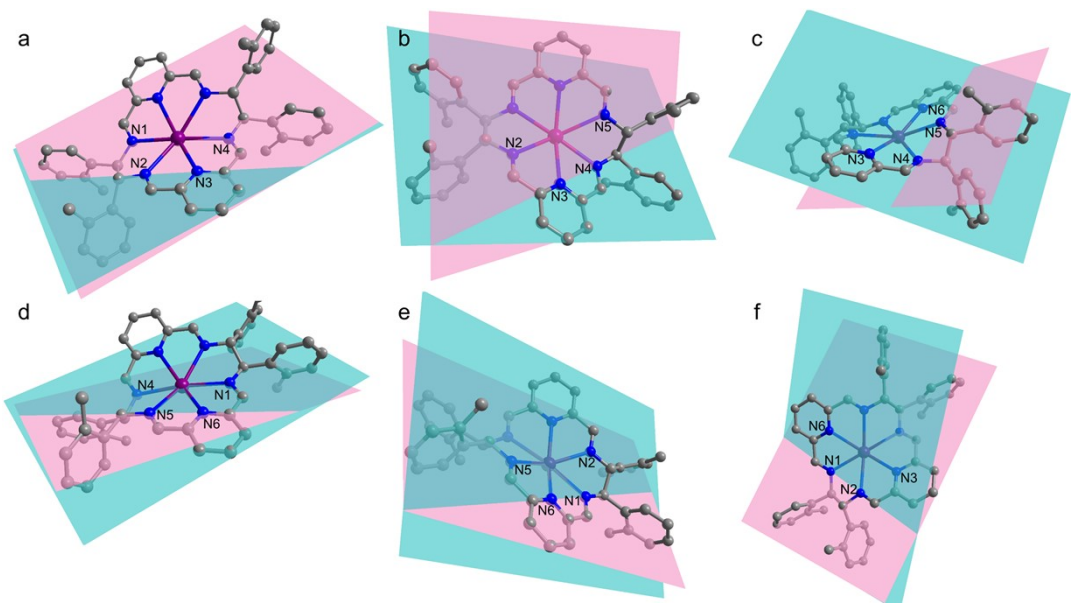

Fig. S9 Dihedral angles (°) in equatorial hexaazamacrocycle for [Dy($L^{2\text{-}Me}_R$)F_2(H_2O)][BPh_4][9]: (a) N1-N2-N3-N4: 5.07, (b) N2-N3-N4-N5: 44.15, (c) N3-N4-N5-N6: 48.28, (d) N4-N5-N6-N1: 15.30, (e) N5-N6-N1-N2: 24.23, (f) N6-N1-N2-N3: 29.19. Note for example that the dihedral angle N1-N2-N3-N4 is the angle between the N1N2N3 plane and the N2N3N4 plane. Dy, violet; C, grey; N, blue.

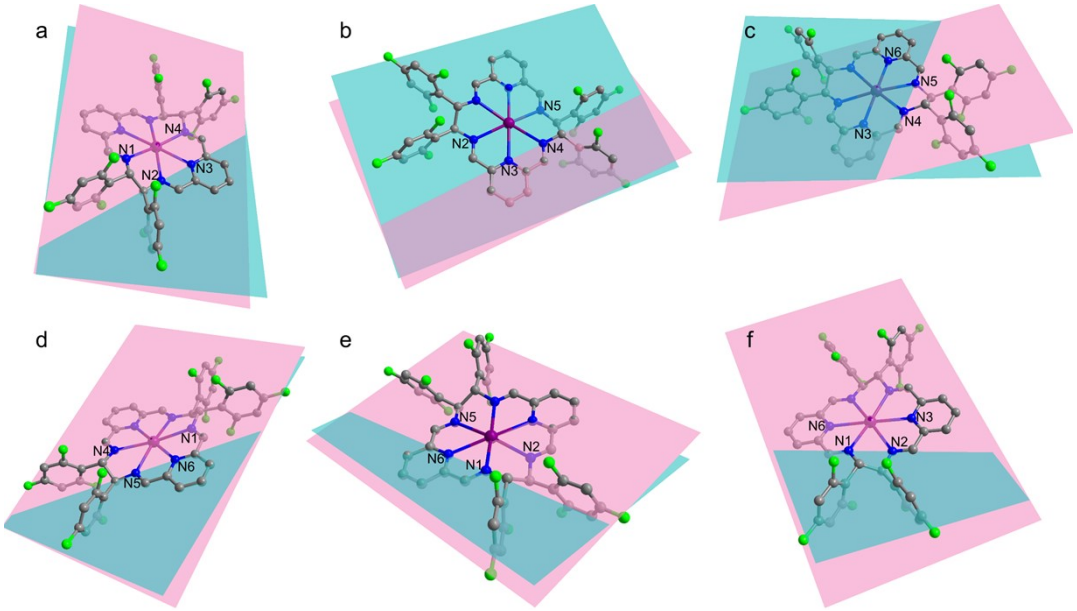

Fig. S10 Dihedral angles (°) in equatorial hexaazamacrocycle for [Dy(L^{F}_R)(Ph_3SiO)$_2$][PF_6][10]: (a) N1-N2-N3-N4: 8.28, (b) N2-N3-N4-N5: 12.46, (c) N3-N4-N5-N6: 21.06, (d) N4-N5-N6-N1: 9.50, (e) N5-N6-N1-N2: 11.22, (f) N6-N1-N2-N3: 19.88. Note for example that the dihedral angle N1-N2-N3-N4 is the angle between the N1N2N3 plane and the N2N3N4 plane. Dy, violet; C, grey; N, blue; F, bright green.

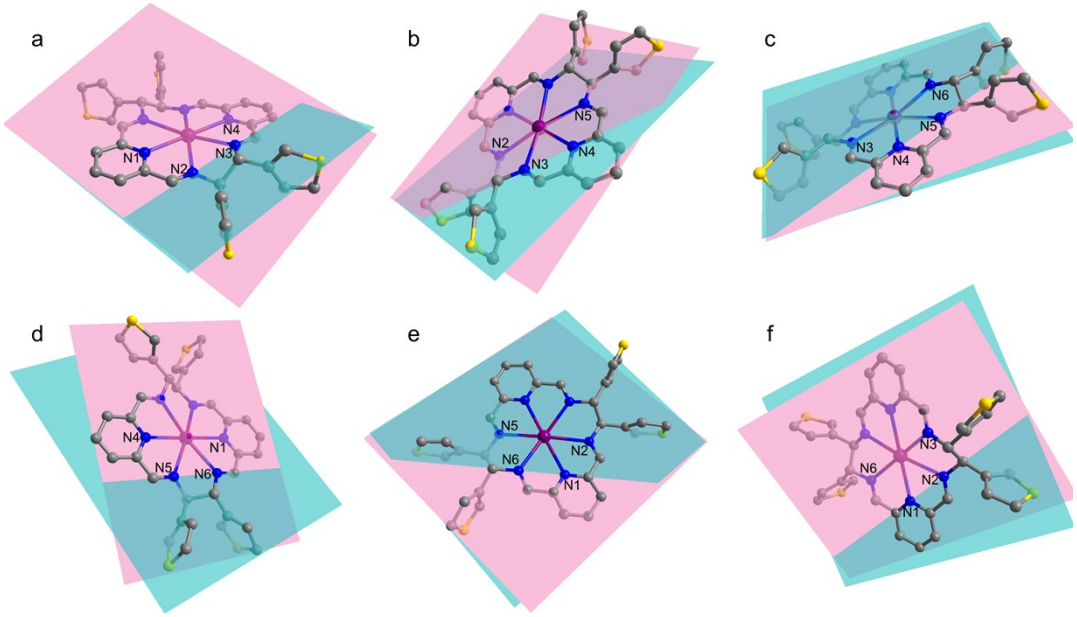

Fig. S11 Dihedral angles (°) in equatorial hexaazamacrocycle for **1**: (a) N1-N2-N3-N4: 28.39, (b) N2-N3-N4-N5: 17.26, (c) N3-N4-N5-N6: 6.21, (d) N4-N5-N6-N1: 17.58, (e) N5-N6-N1-N2: 5.73, (f) N6-N1-N2-N3: 17.19. Note for example that the dihedral angle N1-N2-N3-N4 is the angle between the N1N2N3 plane and the N2N3N4 plane. Dy, violet; C, grey; N, blue; S, yellow.

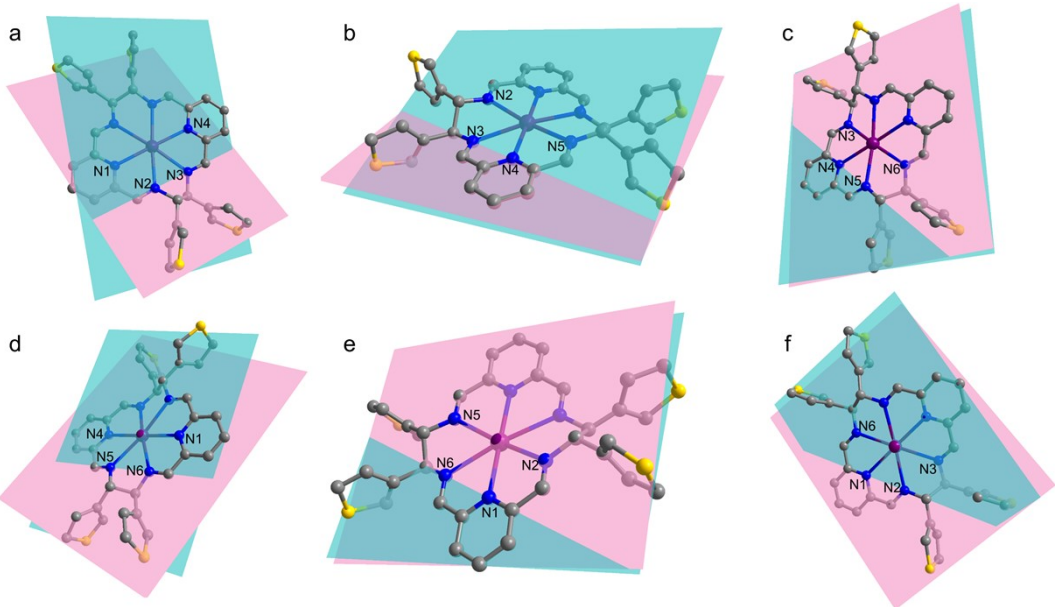

Fig. S12 Dihedral angles (°) in equatorial hexaazamacrocycle for **2**: (a) N1-N2-N3-N4: 29.30, (b) N2-N3-N4-N5: 18.79, (c) N3-N4-N5-N6: 3.05, (d) N4-N5-N6-N1: 14.46, (e) N5-N6-N1-N2: 3.84, (f) N6-N1-N2-N3: 18.50. Note for example that the dihedral angle N1-N2-N3-N4 is the angle between the N1N2N3 plane and the N2N3N4 plane. Dy, violet; C, grey; N, blue; S, yellow.

Table S4 Axial bond angle and sum of the dihedral angles in equatorial hexaazamacrocycle for selected dysprosium(III) hexaazamacrocyclic SMMs.

Compounds	Axial bond angle / °	Sum of the dihedral angles in equatorial hexaazamacrocycle / °	Ref.
$[Dy(L^{N6})(Ph_3SiO)_2][PF_6]$	179.8 (O-Dy-O)	174.4	5
$[Dy(L^{N6}{}_R)(Ph_3SiO)_2][PF_6]$	178.9 (O-Dy-O)	100.3	6
$[Dy(L^{N6}{}_R)(3ThCOO)_2][BPh_4]$	143.0 (O-Dy-O)	179.7	7
$[Dy(L^{N6}{}_R)([7]helicene)_2][BPh_4]$	165.8 (O-Dy-O)	146.4	8
$[Dy(L^{2\text{-}Me}{}_R)F_2(H_2O)][BPh_4]$	146.4 (F-Dy-F)	165.9	9
$[Dy(L^{F}{}_R)(Ph_3SiO)_2][PF_6]$	178.3 (O-Dy-O)	82.4	10
1	179.4 (O-Dy-O)	92.4	This work
2	179.3 (O-Dy-O)	87.9	This work

Table S5 The CShM values calculated by SHAPE 2.1 for **1** and **2**.[11-12]

Central atom	Coordination Geometry	**1**	**2**
Dy	Octagon (D_{8h})	29.672	29.686
	Heptagonal pyramid (C_{7v})	21.245	21.191
	Hexagonal bipyramid (D_{6h})	**1.424**	**1.379**
	Cube (O_h)	9.415	9.146
	Square antiprism (D_{4d})	16.954	16.737
	Triangular dodecahedron (D_{2d})	14.744	14.514
	Johnson gyrobifastigium J26 (D_{2d})	7.139	7.289
	Johnson elongated triangular bipyramid J14 (D_{3h})	24.184	24.132
	Biaugmented trigonal prism J50 (C_{2v})	15.995	15.830
	Biaugmented trigonal prism (C_{2v})	16.025	15.861
	Snub diphenoid J84 (D_{2d})	15.898	15.777
	Triakis tetrahedron (T_d)	10.176	9.891
	Elongated trigonal bipyramid (D_{3h})	21.904	21.852

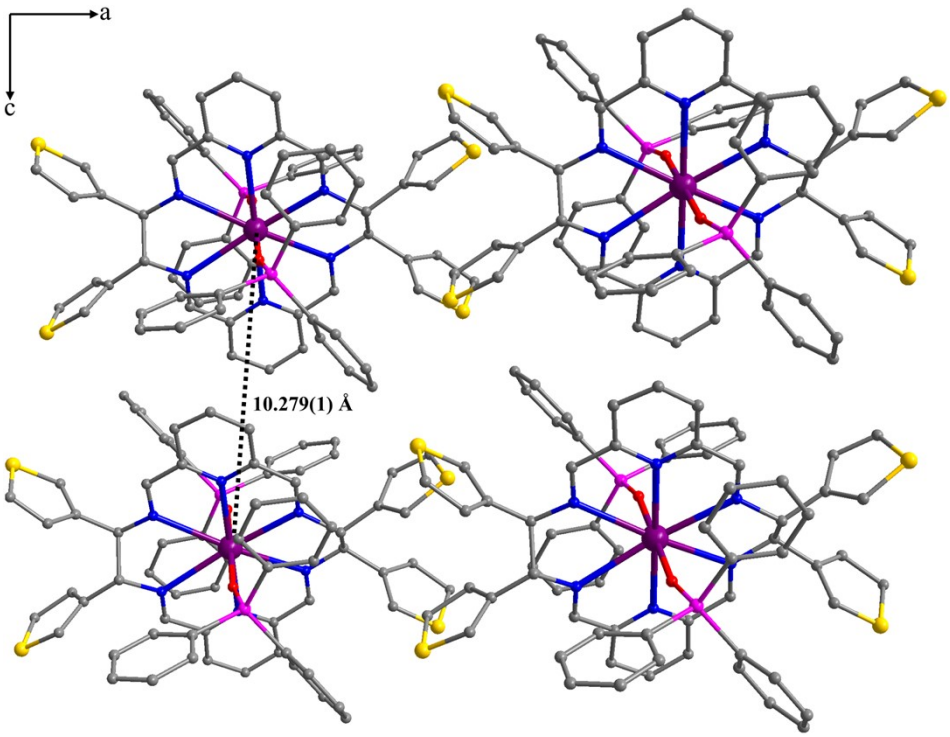

Fig. S13 The packing diagram for **1** viewed along the crystallographic *b* axis with the shortest intermolecular Dy···Dy distance of 10.279(1) Å. Dy, violet; S, yellow; Si, pink; O, red, N; blue; C, grey. H atoms and $[PF_6]^-$ anions are omitted for clarity.

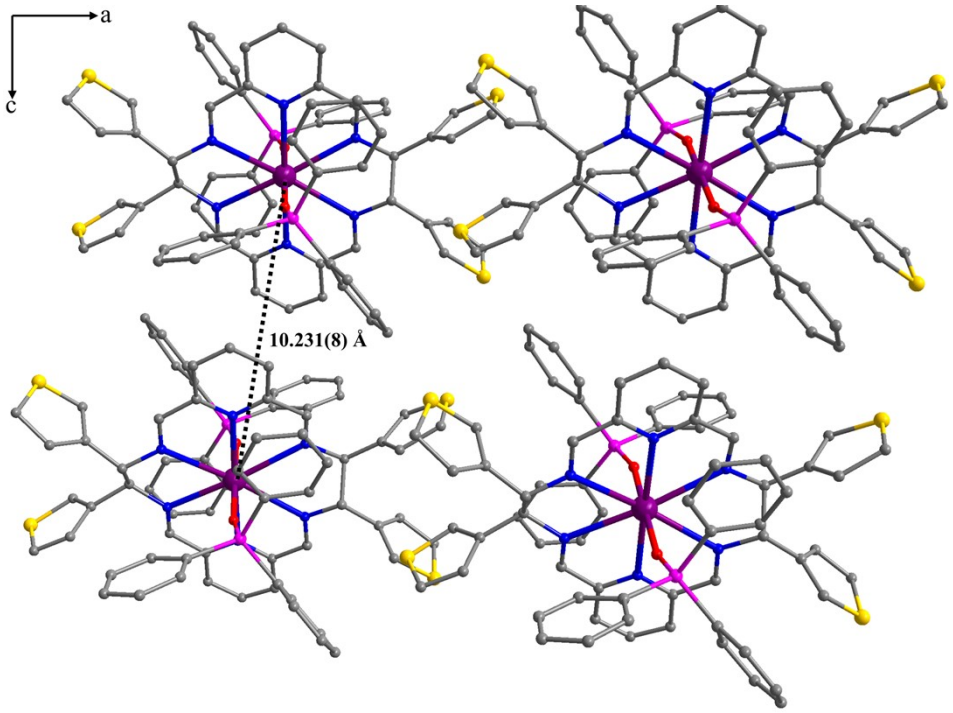

Fig. S14 The packing diagram for **2** viewed along the crystallographic *b* axis with the shortest intermolecular Dy···Dy distance of 10.231(8) Å. Dy, violet; S, yellow; Si, pink; O, red, N; blue; C, grey. H atoms and $[PF_6]^-$ anions are omitted for clarity.

3. Magnetic measurements

Variable-field magnetization data were recorded on a Quantum Design MPMS-XL7 SQUID magnetometer from 0-70 kOe and variable-temperature magnetic susceptibility data were recorded with an external magnetic field of 1000 Oe in the temperature range of 2-300 K. Magnetic hysteresis loops were measured using a Quantum Design MPMS3 magnetometer between ±70 kOe at an average sweep rate of 200 Oe s^{-1}. Alternating current (ac) magnetic susceptibility measurements were performed using a Quantum Design MPMS3 magnetometer under zero dc field and an oscillating field of 3 Oe. The sample masses for **1** and **2** were 10.45 mg and 9.82 mg, respectively. The experimental magnetic susceptibility data were corrected for the diamagnetism estimated from Pascal's tables and sample holder calibration.[13]

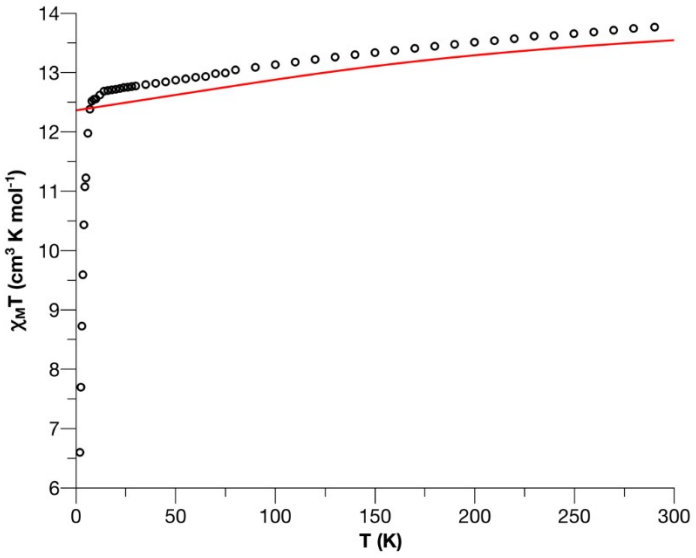

Fig. S15 Temperature dependence of the $\chi_M T$ values at 1000 Oe calculated (full lines) and measured for **1** (empty circles).

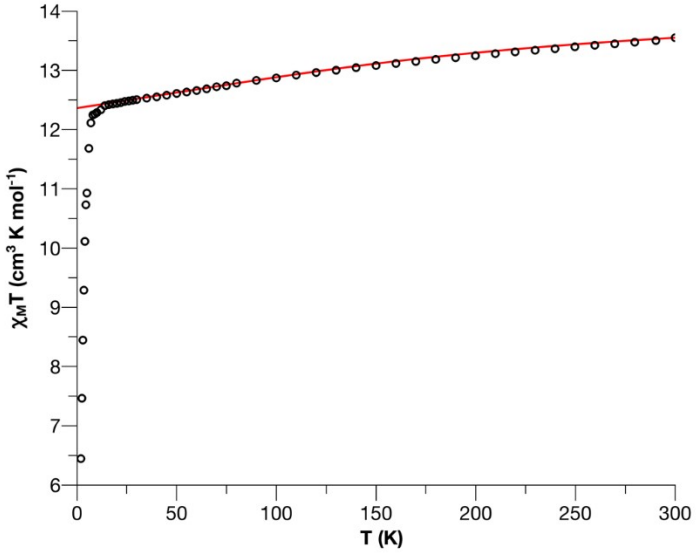

Fig. S16 Temperature dependence of the $\chi_M T$ values at 1000 Oe calculated (full lines) and measured for **2** (empty circles).

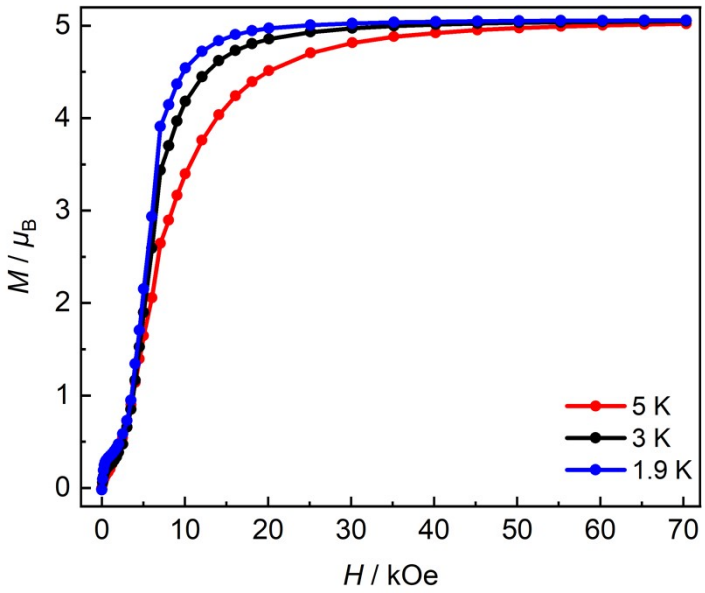

Fig. S17 Field dependence of the magnetization at 5, 3, and 1.9 K for **1**.

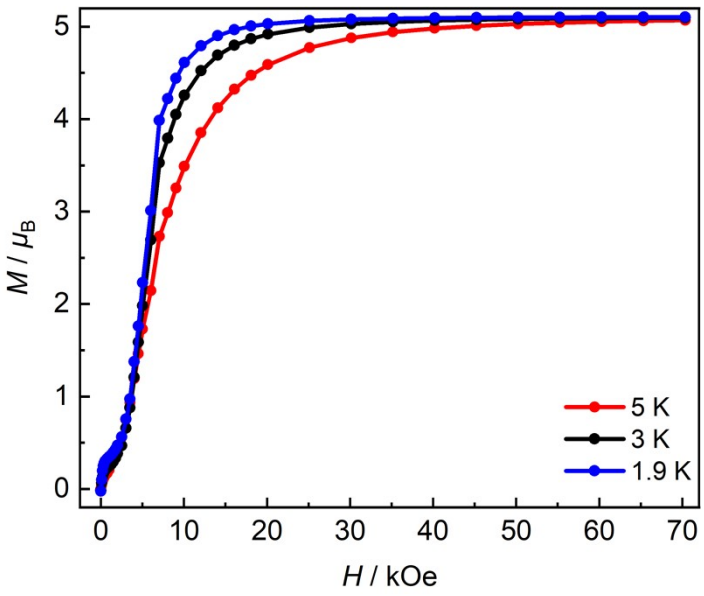

Fig. S18 Field dependence of the magnetization at 5, 3, and 1.9 K for **2**.

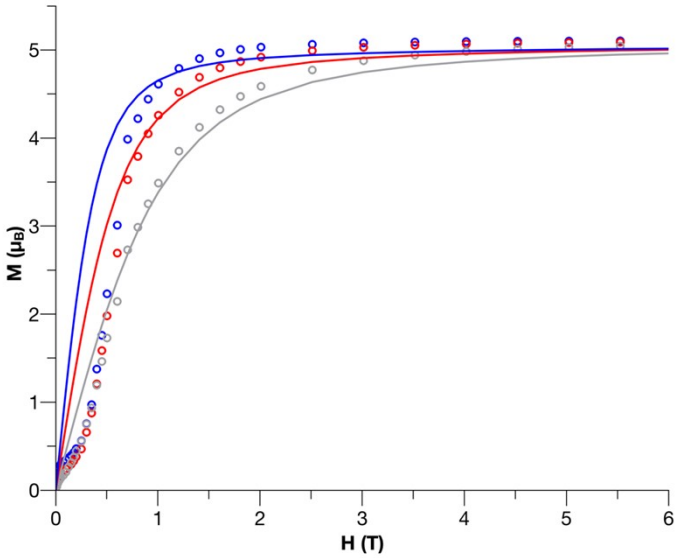

Fig. S19 Field dependences of magnetization in the field range 0-6 T at 5, 3, and 1.9 K for **1**. Solid lines correspond to the *ab initio* calculations.

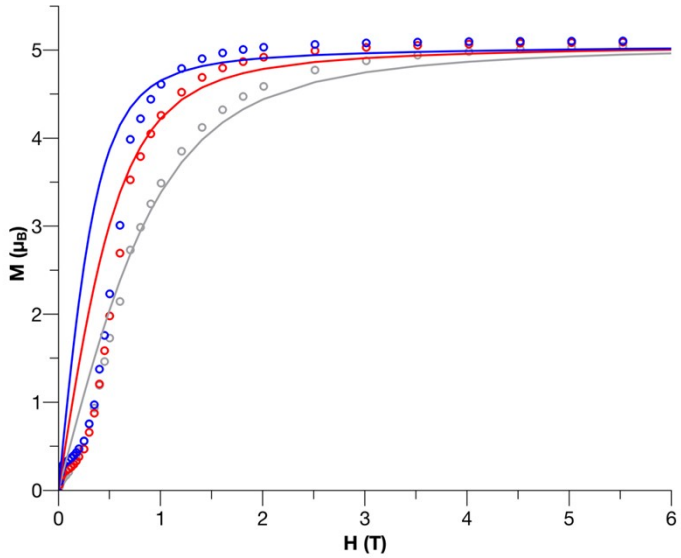

Fig. S20 Field dependences of magnetization in the field range 0-6 T at 5, 3, and 1.9 K for **2**. Solid lines correspond to the *ab initio* calculations.

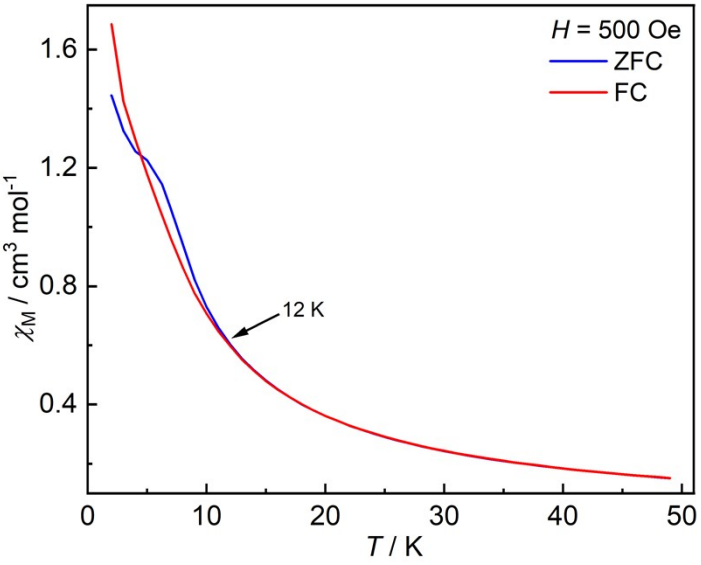

Fig. S21 The zero-field-cooled (ZFC) and field-cooled (FC) magnetic susceptibility data for **1** collected at an applied field of 500 Oe.

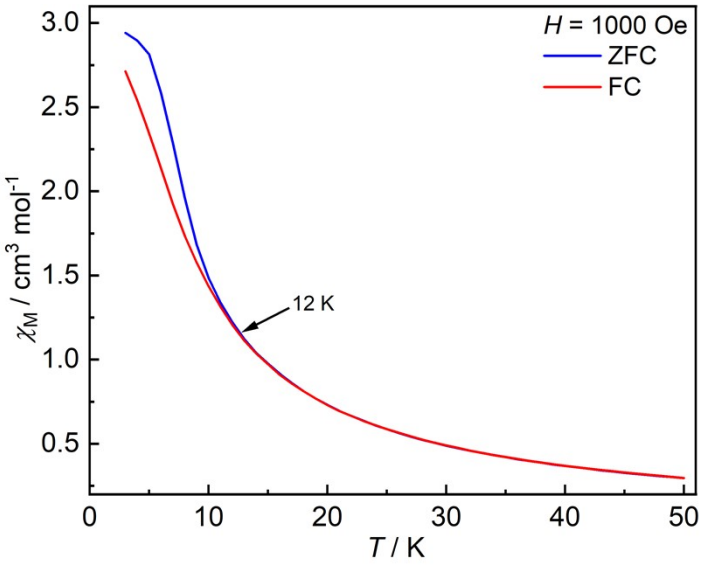

Fig. S22 The zero-field-cooled (ZFC) and field-cooled (FC) magnetic susceptibility data for **1** collected at an applied field of 1000 Oe.

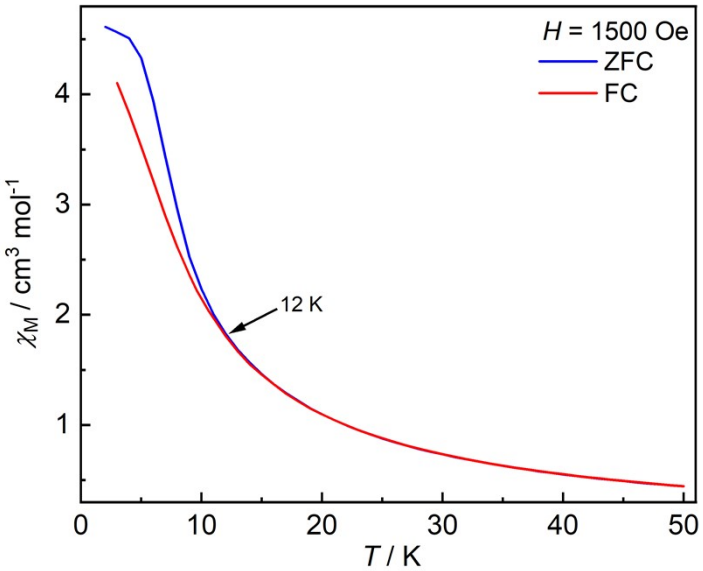

Fig. S23 The zero-field-cooled (ZFC) and field-cooled (FC) magnetic susceptibility data for **1** collected at an applied field of 1500 Oe.

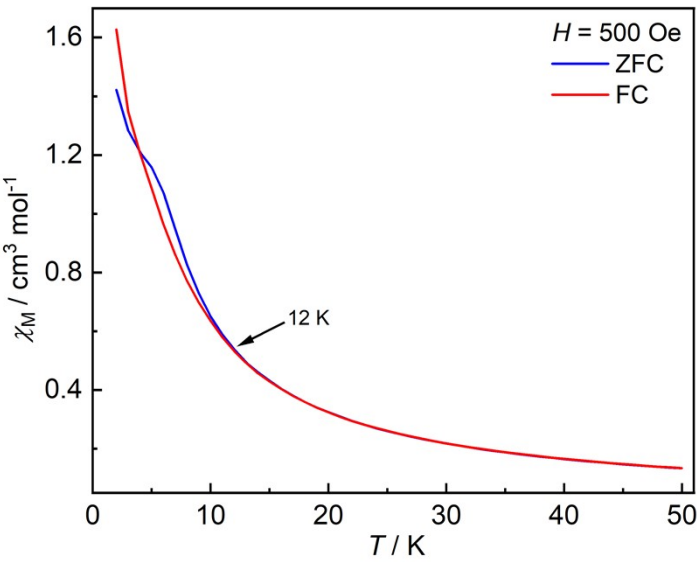

Fig. S24 The zero-field-cooled (ZFC) and field-cooled (FC) magnetic susceptibility data for **2** collected at an applied field of 500 Oe.

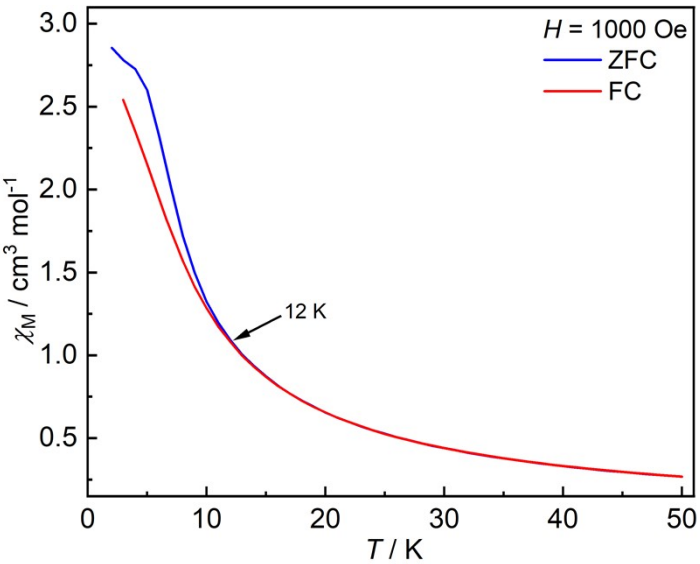

Fig. S25 The zero-field-cooled (ZFC) and field-cooled (FC) magnetic susceptibility data for **2** collected at an applied field of 1000 Oe.

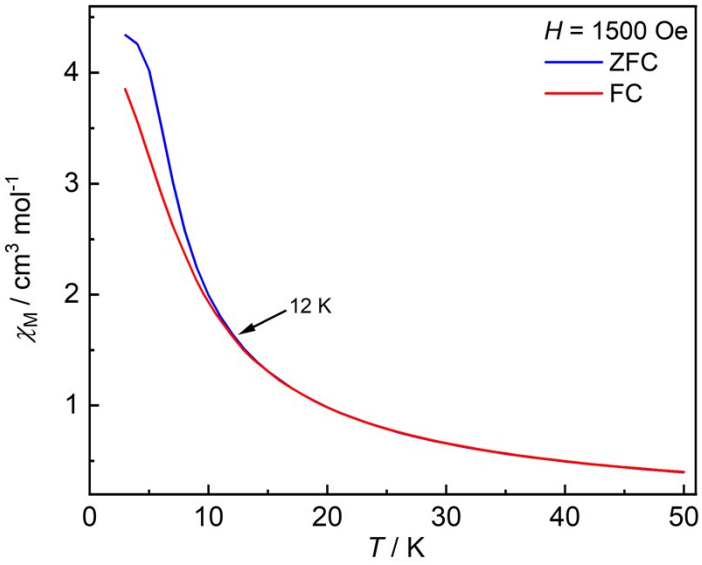

Fig. S26 The zero-field-cooled (ZFC) and field-cooled (FC) magnetic susceptibility data for **2** collected at an applied field of 1500 Oe.

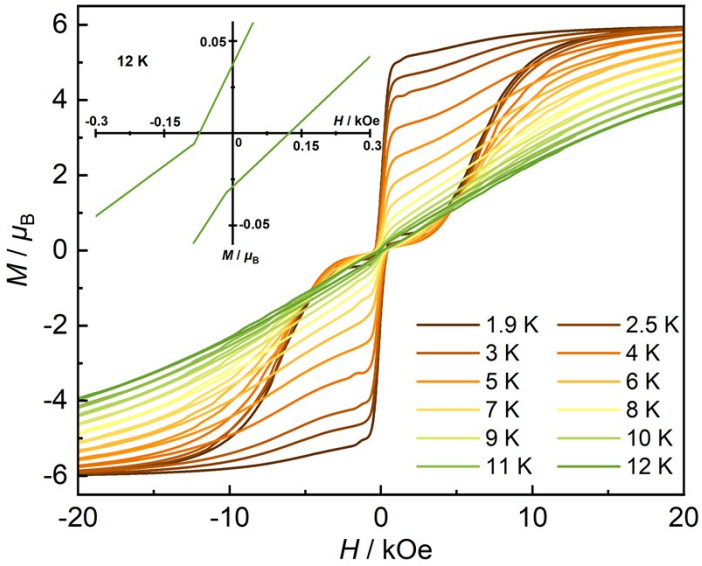

Fig. S27 Magnetic hysteresis loops for **2** at 1.9-12 K using an average sweep rate of 200 Oe s^{-1}. (inset) Expansion of magnetic hysteresis loop for **2** at 12 K.

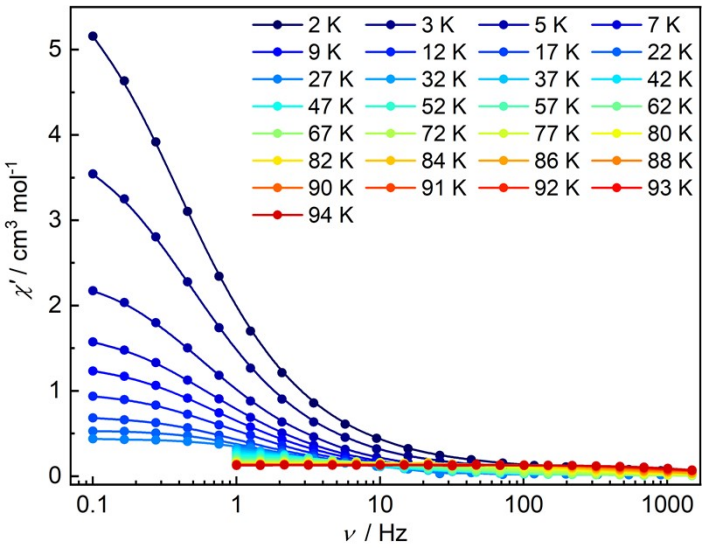

Fig. S28 $\chi'(\nu)$ plots for **1** in the temperature range of 2-94 K under zero dc field.

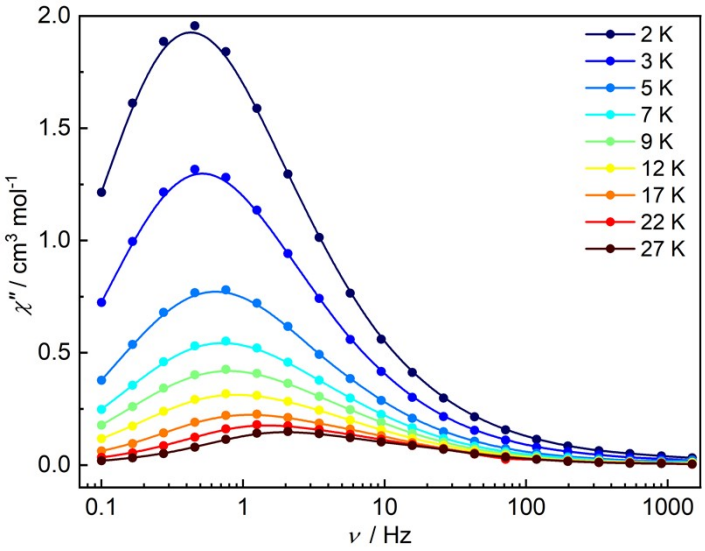

Fig. S29 $\chi''(\nu)$ plots for **1** in the temperature range of 2-27 K under zero dc field.

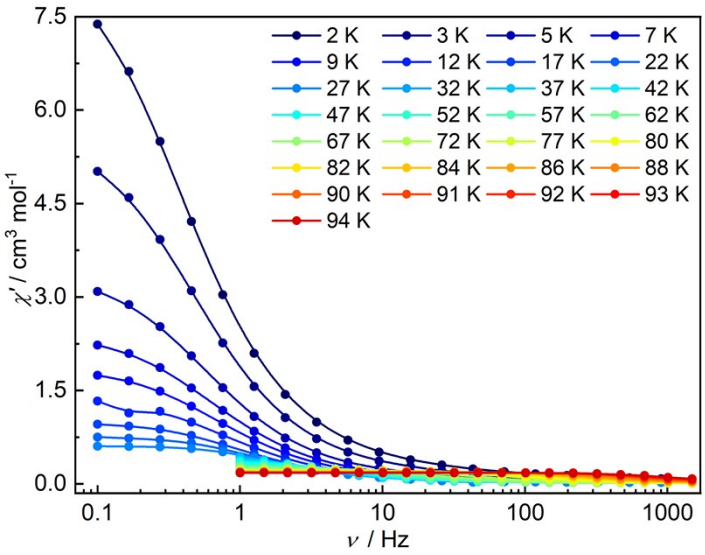

Fig. S30 $\chi'(\nu)$ plots for **2** in the temperature range of 2-94 K under zero dc field.

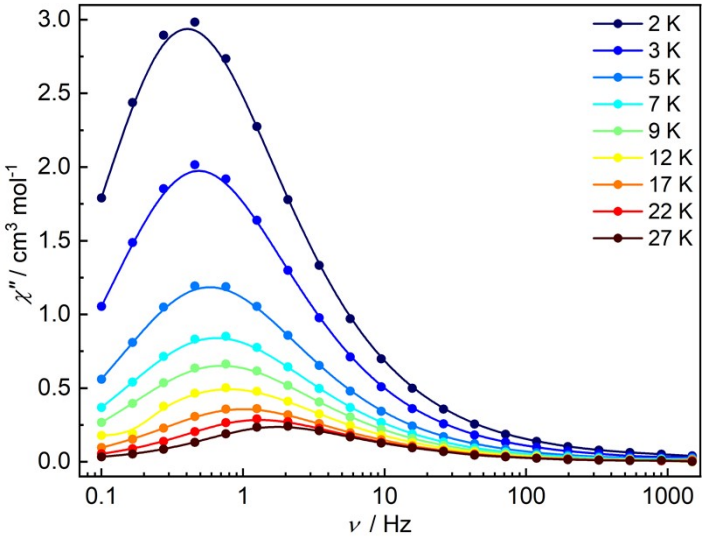

Fig. S31 $\chi''(\nu)$ plots for **2** in the temperature range of 2-27 K under zero dc field.

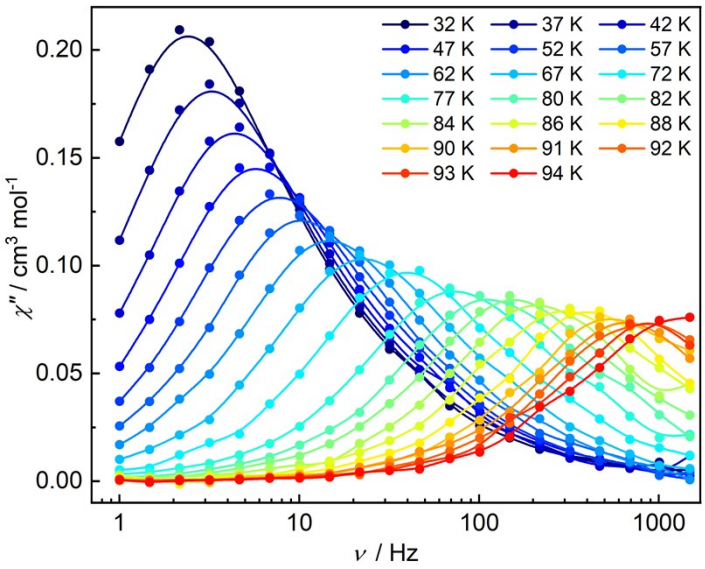

Fig. S32 $\chi''(\nu)$ plots for **2** in the temperature range of 32-94 K under zero dc field.

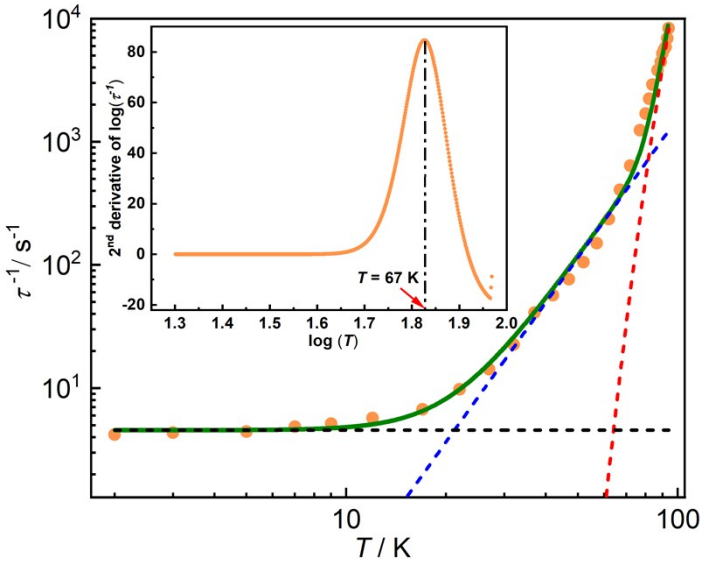

Fig. S33 Temperature dependence of the magnetization reversal rate (τ^{-1}) for **1**. The red, blue, and black dash lines represent the Orbach, Raman, and QTM relaxation processes, respectively; the green solid line represents the fit to $\tau^{-1} = \tau_0^{-1}\exp(-U_{eff}/k_BT) + CT^n + \tau_{QTM}^{-1}$, giving U_{eff} = 1510(60) K, τ_0 = 1.28(2) × 10^{-11} s, C = 4.69(3) × 10^{-5} s^{-1} K^{-n}, n = 3.7(2), τ_{QTM} = 0.22(2) s, R^2 = 0.995. (inset) Second derivative of the plot log(τ^{-1}) *vs.* log(T). The maximum indicates the temperature at which the Raman relaxation mechanism becomes dominant over the Orbach process.

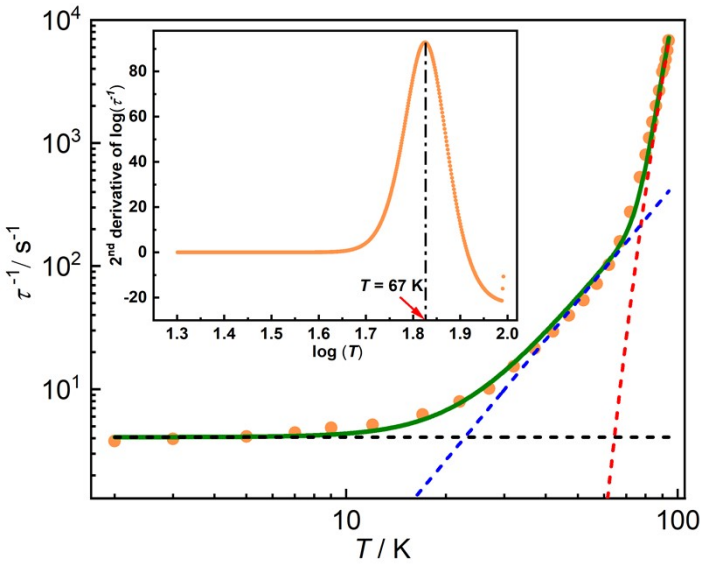

Fig. S34 Temperature dependence of the magnetization reversal rate (τ^{-1}) for **2**. The red, blue, and black dash lines represent the Orbach, Raman, and QTM relaxation processes, respectively; the green solid line represents the fit to $\tau^{-1} = \tau_0^{-1}\exp(-U_{eff}/k_BT) + CT^n + \tau_{QTM}^{-1}$, giving U_{eff} = 1519(52) K, τ_0 = 1.42(1) × 10^{-11} s, C = 1.58(3) × 10^{-4} s^{-1} K^{-n}, n = 3.2(2), τ_{QTM} = 0.24(2) s, R^2 = 0.996. (inset) Second derivative of the plot log(τ^{-1}) *vs*. log(T). The maximum indicates the temperature at which the Raman relaxation mechanism becomes dominant over the Orbach process.

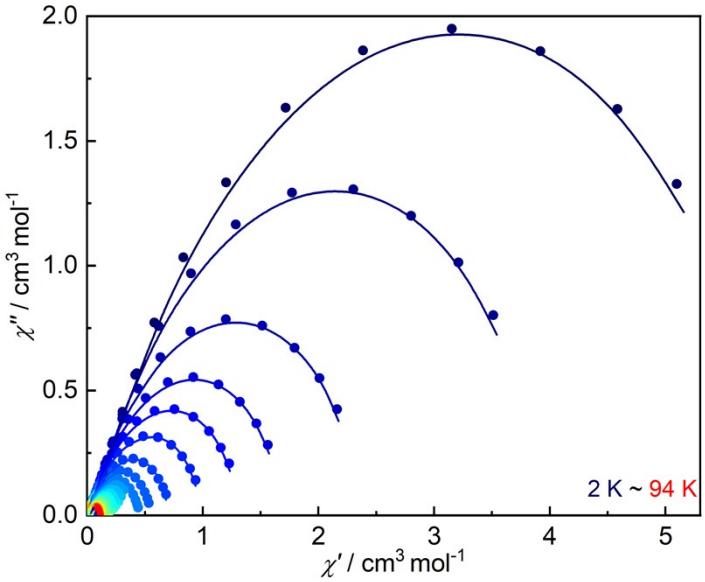

Fig. S35 Cole-Cole plots for **1**. The solid lines are obtained by fitting experimental data to generalized Debye model.[14]

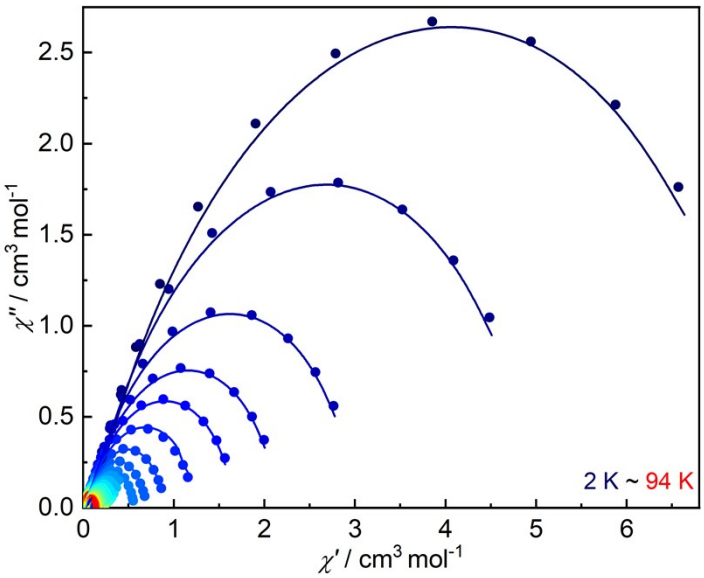

Fig. S36 Cole-Cole plots for **2**. The solid lines are obtained by fitting experimental data to generalized Debye model.[14]

Table S6 The relaxation fitting parameters for **1** from fitting ac data at varying temperatures.

T (K)	χ_S (cm^3 mol^{-1})	χ_T (cm^3 mol^{-1})	τ (s)	α
2	0.08293	6.20756	0.23865	0.27839
3	0.06436	4.11659	0.23015	0.26635
5	0.04316	2.46215	0.22542	0.26610
7	0.03202	1.76096	0.20632	0.27401
9	0.02566	1.37334	0.19462	0.28079
12	0.02017	1.03369	0.17518	0.28524
17	0.01836	0.73469	0.14893	0.27952
22	0.01297	0.56093	0.10233	0.25838
27	0.01472	0.45532	0.07037	0.24137
32	0.1101	0.41937	0.04434	0.29453
37	0.01159	0.35488	0.02436	0.27200
42	0.01231	0.30421	0.01767	0.24093
47	0.01020	0.27038	0.01306	0.23348
52	0.01031	0.24205	0.00952	0.21714
57	0.00924	0.21817	0.00666	0.20762
62	0.00813	0.20039	0.00425	0.20198
67	0.00111	0.18260	0.00246	0.16721
72	0.00895	0.17048	0.00157	0.18691
77	0.01200	0.15898	8.0905E-4	0.16313
80	0.01441	0.15046	5.9268E-4	0.16216
82	0.01633	0.14685	4.4908E-4	0.16526
84	0.01495	0.14436	3.4393E-4	0.15234
86	0.01989	0.14062	2.6369E-4	0.11903
88	0.02720	0.13635	2.2463E-4	0.11285
90	0.03261	0.13372	1.8608E-4	0.06857
91	0.02984	0.13165	1.7851E-4	0.06639
92	0.03255	0.13066	1.7029E-4	0.06383
93	0.04396	0.12836	1.4446E-4	0.07606
94	0.04272	0.12801	1.2010E-4	0.08532

Table S7 The relaxation fitting parameters for **2** from fitting ac data at varying temperatures.

T (K)	χ_S (cm^3 mol^{-1})	χ_T (cm^3 mol^{-1})	τ (s)	α
2	0.12058	7.84749	0.26413	0.22951
3	0.09230	5.15859	0.25286	0.21590
5	0.06543	3.09527	0.24258	0.21012
7	0.04775	2.21075	0.22555	0.21328
9	0.04029	1.71850	0.20636	0.21389
12	0.03434	1.23789	0.19448	0.19751
17	0.02891	0.91257	0.16054	0.19327
22	0.02548	0.70153	0.12586	0.17066
27	0.02225	0.56383	0.09879	0.14369
32	0.01792	0.50804	0.06513	0.17606
37	0.01599	0.43131	0.04659	0.15643
42	0.01619	0.37332	0.03396	0.13731
47	0.01452	0.33187	0.02521	0.12319
52	0.01445	0.29782	0.01891	0.11303
57	0.01346	0.27028	0.01392	0.10355
62	0.01327	0.24646	0.00975	0.09904
67	0.01215	0.22852	0.00632	0.09637
72	0.01070	0.21213	0.00363	0.09170
77	0.01135	0.19733	0.0019	0.09072
80	0.01553	0.18897	0.00125	0.06979
82	0.01546	0.18454	9.1303E-4	0.06949
84	0.01574	0.17997	6.7482E-4	0.07043
86	0.01699	0.17571	5.0014E-4	0.05848
88	0.02271	0.17039	3.7515E-4	0.03328
90	0.02048	0.16753	2.6475E-4	0.03615
91	0.02614	0.16459	2.4329E-4	0.02124
92	0.02003	0.16326	2.0973E-4	0.04584
93	0.02796	0.16206	1.7687E-4	0.01979
94	0.01544	0.15997	1.4688E-4	0.03626

4. *Ab initio* calculations

Atomic positions were extracted from the crystal structures obtained by X-ray diffraction for **1** and **2**. Only the positions of the hydrogen atoms were optimized at the DFT level using the 2019 release of the Amsterdam Density Functional (ADF) package,[15-17] while other atom positions were kept frozen. The calculations employed the revPBE functional,[18-19] the triple-ζ polarized all-electron Slater type basis (TZP) from the ADF basis-set library, used the scalar relativistic (SR) all-electron zeroth-order regular approximation (ZORA) Hamiltonian and were performed in the unrestricted formalism by considering an open-shell octet spin state.[20]

All wave function-based calculations were performed using the State-Averaged Complete Active Space Self-Consistent Field approach with Restricted-Active-Space-State-Interaction method (SA-CASSCF/RASSI-SO), as implemented in the *OpenMolcas* quantum-chemistry package (version 19.11).[21] In this approach, the relativistic effects are treated in two steps on the basis of the Douglas–Kroll Hamiltonian.[22] The scalar terms are included in the basis-set generation and are used to determine the CASSCF wave functions and energies.[23] Spin-orbit coupling is then added within the RASSI-SO method, which mixes the calculated CASSCF spin free wave functions.[24-25] Spin-orbit (SO) integrals are calculated using the AMFI (atomic mean-field integrals) approximation.[26] The resulting spin-orbit wave functions and energies are used to compute the magnetic properties and g-tensors of the ground state and excited states multiplts following the pseudospin $\tilde{S} = 1/2$ formalism, as implemented in the SINGLE_ANISO routine.[27] Cholesky decomposition of the bioelectronic integrals was employed to save disk space and to speed up the calculations.[28] The active space consisted of the nine 4f electrons of the Dy^{III} ions spanning the seven 4f orbitals; CAS(9,7) SCF.

State-averaged CASSCF calculations were performed for all of the sextets (21 roots), all the quartets (224 roots), 300 out of the 490 doublets of the Dy^{III} ions. In RASSI-SO, roots were mixed through spin–orbit coupling, 21 sextets, 224 quartets, 300 doublets. All atoms were described by ANO-RCC basis set. The following contractions were used: [8s7p5d3f2g1h] for the Dy, [4s3p2d1f] for the Si, S, N and O atoms, [3s2p1d] for the C atoms and [2s] for the H atoms.[29-30]

Table S8 Computed energy (the ground state is set at zero), main components (> 10%) of the wavefunction and composition of the *g*-tensor (g_x, g_y, g_z) for each state of the ground-state multiplet $^6H_{15/2}$ in **1** (CAS(8,7)SCF-RASSI-SO level).

	[Dy(L^{Thp}_R)($Ph_3SiO)_2$][PF_6] (**1**)				
KD	**Energy (cm^{-1})**		***g***		**Wavefunction**
1	0.0	0.0	0.0	19.9	100.0% |±15/2>
2	473.1	0.1	0.1	17.0	99.5% |±13/2>
3	876.8	0.1	0.6	13.5	93.6% |±11/2>
4	1051.6	0.5	1.6	16.3	49.1% |±1/2> + 35.5% |±3/2>
5	1101.2	1.2	4.6	9.8	36.3% |±9/2> + 23.4% |±1/2> + 16.7% |±5/2> + 15.4% |±3/2>
6	1195.2	0.3	2.4	12.8	26.5% |±5/2> + 26.4% |±7/2> + 25.0% |±9/2> + 15.5% |±3/2>
7	1228.0	2.0	3.6	10.0	26.4% |±3/2> + 24.6% |±9/2> + 19.9% |±5/2> + 14.9% |±1/2> + 13.6% |±7/2>
8	1345.7	1.6	2.6	16.0	51.1% |±7/2> + 32.6% |±5/2>

Table S9 Computed energy (the ground state is set at zero), main components (>10%) of the wavefunction and composition of the *g*-tensor (g_x, g_y, g_z) for each state of the ground-state multiplet $^6H_{15/2}$ in **2** (CAS(8,7)SCF-RASSI-SO level).

	[Dy(L^{Thp}_S)($Ph_3SiO)_2$][PF_6] (**2**)				
KD	**Energy (cm^{-1})**		***g***		**Wavefunction**
1	0.0	0.0	0.0	19.9	100.0% |±15/2>
2	468.4	0.1	0.1	17.0	99.5% |±13/2>
3	866.1	0.0	0.6	13.4	93.3% |±11/2>
4	1036.5	0.6	1.7	16.1	49.3% |±1/2> + 36.0% |±3/2>
5	1084.2	0.8	4.4	9.6	35.0% |±9/2> + 23.9% |±1/2> + 16.8% |±5/2> + 16.1% |±3/2>
6	1176.6	0.4	2.4	13.4	29.9% |±5/2> + 27.6% |±7/2> + 22.0% |±9/2> + 13.8% |±3/2>
7	1208.0	2.2	3.5	9.4	29.0% |±9/2> + 27.4% |±3/2> + 17.2% |±5/2> + 13.9% |±1/2> + 11.8% |±7/2>
8	1324.0	1.7	2.7	15.9	52.0% |±7/2> + 32.4% |±5/2>

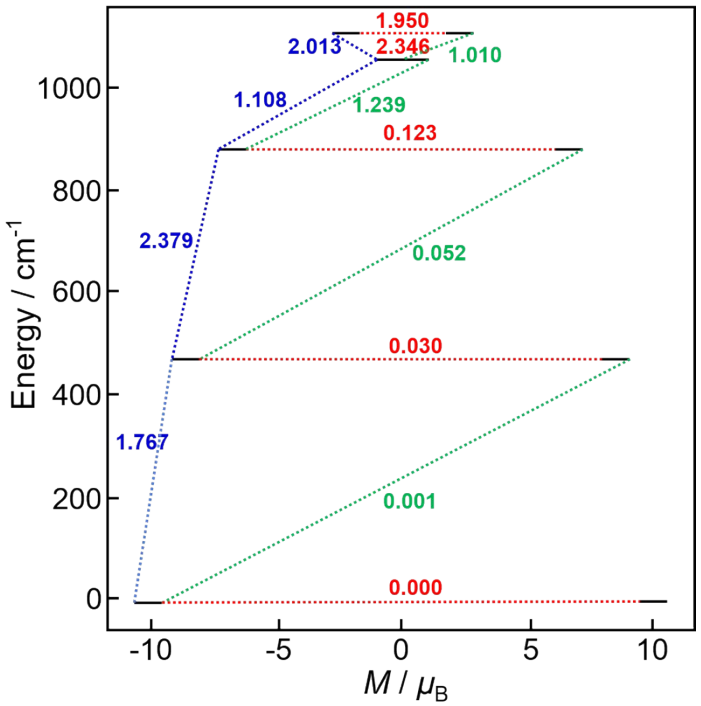

Fig. S37 Calculated magnetization blocking barrier of the Dy centre for **2**. Only the fifth lowest KDs (thick black lines) are represented according to their magnetic moment along the main magnetic axis. The blue dashed lines represent vertical excitations; the green dashed lines correspond to possible Orbach relaxation processes while the red dashed lines correspond to QTM/TA-QTM processes. The values correspond to the mean value of the corresponding transversal matrix element of the transition magnetic moment.

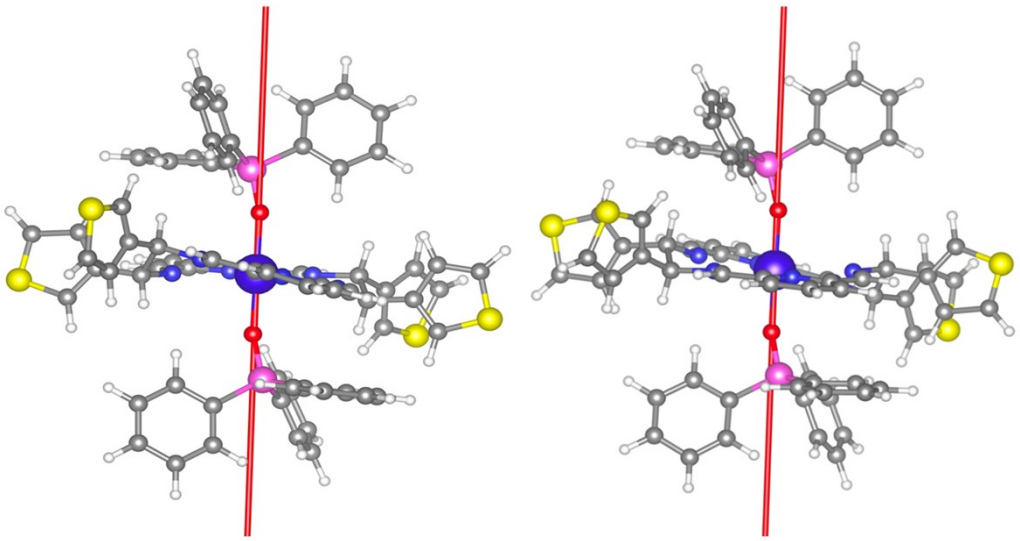

Fig. S38 Ground-state anisotropy axes (red) of **1** (left) and **2** (right). Color codes: Dy, purple; S, yellow; Si, pink; O, red, N, blue; C, grey; and H, white.

5. References

1 M. Zhou, K. Li, D. Chen, R. Xu, G. Xu and W. Tang, *J. Am. Chem. Soc.*, 2020, **142**, 10337-10342.

2 O. V. Dolomanov, L. J. Bourhis, R. J. Gildea, J. A. K. Howard and H. Puschmann, *J. Appl. Crystallogr.*, 2009, **42**, 339-341.

3 G. Sheldrick, *Acta Crystallogr. C Struct. Chem.*, 2015, **71**, 3-8.

4 G. Sheldrick, *Acta Crystallogr. A Found. Adv.*, 2015, **71**, 3-8.

5 A. B. Canaj, S. Dey, E. R. Martí, C. Wilson, G. Rajaraman and M. Murrie, *Angew. Chem. Int. Ed.*, 2019, **58**, 14146-14151.

6 M. S. Raju, K. Paillot, I. Breslavetz, G. Novitchi, G. L. J. A. Rikken, C. Train and M. Atzori, *J. Am. Chem. Soc.*, 2024, **146**, 23616-23624.

7 Q. Zhou, N. Maqsood, T. Feng, X.-L. Li, P. Zhang and J. Tang, *Inorg. Chem.*, 2025, **64**, 16036-16044.

8 Z. Zhu, T. Wang, L. A. Mariano, S. Paul, W. Wernsdorfer, A. Lunghi and J. Tang, *J. Am. Chem. Soc.*, 2025, **147**, 42815–42824.

9 J. Wu, G.-L. Wang, Z. Zhu, C. Zhao, X.-L. Li, Y.-Q. Zhang and J. Tang, *Chem. Commun.*, 2022, **58**, 7638-7641.

10 Z. Zhu, C. Zhao, T. Feng, X. Liu, X. Ying, X.-L. Li, Y.-Q. Zhang and J. Tang, *J. Am. Chem. Soc.*, 2021, **143**, 10077-10082.

11 M. Pinsky and D. Avnir, *Inorg. Chem.*, 1998, **37**, 5575-5582.

12 D. Casanova, J. Cirera, M. Llunell, P. Alemany, D. Avnir and S. Alvarez, *J. Am. Chem. Soc.*, 2004, **126**, 1755-1763.

13 E. A. L. Boudreaux and L. N. Mulay, *Theory and applications of molecular paramagnetism*, John Wiley & Sons, New York, 1976.

14 K. S. Cole and R. H. Cole, *J. Chem. Phys.*, 1941, **9**, 341-351.

15 G. te Velde, F. M. Bickelhaupt, E. J. Baerends, C. Fonseca Guerra, S. J. A. van Gisbergen, J. G. Snijders and T. Ziegler, *J. Comput. Chem.*, 2001, **22**, 931-967.

16 C. Fonseca Guerra, J. G. Snijders, G. te Velde and E. J. Baerends, *Theor. Chem. Acc.*, 1998, **99**, 391-403.

17 Amsterdam Density Functional (ADF), SCM Theoretical Chemistry, https://www.scm.com/).

18 J. P. Perdew, K. Burke and M. Ernzerhof, *Phys. Rev. Lett.*, 1996, **77**, 3865-3868.

19 M. Ernzerhof and G. E. Scuseria, *J. Chem.Phys.*, 1999, **110**, 5029-5036.

20 E. V. Lenthe, E. J. Baerends and J. G. Snijders, *J. Chem.Phys.*, 1993, **99**, 4597-4610.

21 I. Fdez. Galván, M. Vacher, A. Alavi, C. Angeli, F. Aquilante, J. Autschbach, J. J. Bao, S. I. Bokarev, N. A. Bogdanov, R. K. Carlson, L. F. Chibotaru, J. Creutzberg, N. Dattani, M. G. Delcey, S. S. Dong, A. Dreuw, L. Freitag, L. M. Frutos, L. Gagliardi, F. Gendron, A. Giussani, L. González, G. Grell, M. Guo, C. E. Hoyer, M. Johansson, S. Keller, S. Knecht, G. Kovačević, E. Källman, G. Li Manni, M. Lundberg, Y. Ma, S. Mai, J. P. Malhado, P. Å. Malmqvist, P. Marquetand, S. A. Mewes, J. Norell, M. Olivucci, M. Oppel, Q. M. Phung, K. Pierloot, F. Plasser, M. Reiher, A. M. Sand, I. Schapiro, P. Sharma, C. J. Stein, L. K. Sørensen, D. G. Truhlar, M. Ugandi, L. Ungur, A. Valentini, S. Vancoillie, V. Veryazov, O. Weser,

T. A. Wesołowski, P.-O. Widmark, S. Wouters, A. Zech, J. P. Zobel and R. Lindh, *J. Chem. Theory Comput.*, 2019, **15**, 5925-5964.
22 B. A. Hess, *Phys.Rev. A*, 1986, **33**, 3742-3748.
23 B. O. Roos, P. R. Taylor and P. E. M. Sigbahn, *Chem. Phys.*, 1980, **48**, 157-173.
24 P. Å. Malmqvist, B. O. Roos and B. Schimmelpfennig, *Chem. Phys. Lett.*, 2002, **357**, 230-240.
25 P.-Å. Malmqvist and B. O. Roos, *Chem. Phys. Lett.*, 1989, **155**, 189-194.
26 B. A. Heß, C. M. Marian, U. Wahlgren and O. Gropen, *Chem. Phys. Lett.*, 1996, **251**, 365-371.
27 L. F. Chibotaru and L. Ungur, *J. Chem. Phys.*, 2012, **137**, 064112.
28 L. Ungur, W. Van den Heuvel and L. F. Chibotaru, *New J. Chem.*, 2009, **33**, 1224-1230.
29 B. O. Roos, R. Lindh, P.-Å. Malmqvist, V. Veryazov and P.-O. Widmark, *J. Phys. Chem. A*, 2004, **108**, 2851-2858.
30 B. O. Roos, R. Lindh, P.-Å. Malmqvist, V. Veryazov, P.-O. Widmark and A. C. Borin, *J. Phys. Chem. A*, 2008, **112**, 11431-11435.